The Astrophysical Journal, 922:188 (11pp), 2021 December 1 https://doi.org/10.3847/1538-4357/ac28fb

MHD and Ion Kinetic Waves in Field-aligned Flows Observed by Parker Solar Probe

L.-L. Zhao[1,2], G. P. Zank[1,2], J. S. He[3], D. Telloni[4], L. Adhikari[1], M. Nakanotani[1], J. C. Kasper[5,6], and S. D. Bale[7]
[1] Center for Space Plasma and Aeronomic Research (CSPAR), The University of Alabama in Huntsville, Huntsville, AL 35805, USA; lz0009@uah.edu
[2] Department of Space Science, The University of Alabama in Huntsville, Huntsville, AL 35805, USA
[3] School of Earth and Space Sciences, Peking University, Beijing 100871, People's Republic of China
[4] National Institute for Astrophysics Astrophysical Observatory of Torino Via Osservatorio 20, I-10025 Pino Torinese, Italy
[5] BWX Technologies, Inc., Washington, DC 20002, USA
[6] Department of Climate and Space Sciences and Engineering, University of Michigan, Ann Arbor, MI 48109, USA
[7] Physics Department, University of California, Berkeley, CA 94720-7300, USA
Received 2021 June 24; revised 2021 September 11; accepted 2021 September 20; published 2021 November 30

Abstract

Parker Solar Probe (PSP) observed predominately Alfvénic fluctuations in the solar wind near the Sun where the magnetic field tends to be radially aligned. In this paper, two magnetic-field-aligned solar wind flow intervals during PSP's first two orbits are analyzed. Observations of these intervals indicate strong signatures of parallel/antiparallel-propagating waves. We utilize multiple analysis techniques to extract the properties of the observed waves in both magnetohydrodynamic (MHD) and kinetic scales. At the MHD scale, outward-propagating Alfvén waves dominate both intervals, and outward-propagating fast magnetosonic waves present the second-largest contribution in the spectral energy density. At kinetic scales, we identify the circularly polarized plasma waves propagating near the proton gyrofrequency in both intervals. However, the sense of magnetic polarization in the spacecraft frame is observed to be opposite in the two intervals, although they both possess a sunward background magnetic field. The ion-scale plasma wave observed in the first interval can be either an inward-propagating ion cyclotron wave (ICW) or an outward-propagating fast-mode/whistler wave in the plasma frame, while in the second interval it can be explained as an outward ICW or inward fast-mode/whistler wave. The identification of the exact kinetic wave mode is more difficult to confirm owing to the limited plasma data resolution. The presence of ion-scale waves near the Sun suggests that ion cyclotron resonance may be one of the ubiquitous kinetic physical processes associated with small-scale magnetic fluctuations and kinetic instabilities in the inner heliosphere.

Unified Astronomy Thesaurus concepts: Solar wind (1534); Alfven waves (23); Interplanetary turbulence (830); Interplanetary magnetic fields (824)

1. Introduction

Early observations showed that turbulent fluctuations in the solar wind exhibit Alfvén wave-like signatures (Coleman 1967; Belcher & Davis 1971; Goldstein et al. 1995; Tu & Marsch 1995), as indicated by highly correlated velocity and magnetic field fluctuations. These Alfvénic fluctuations are observed to be propagating away from the Sun mostly, i.e., the velocity fluctuations and magnetic field fluctuations are observed to be positively correlated in the inward magnetic sector and negatively correlated in the outward magnetic sector (He et al. 2015). Waves in plasma are characterized by a dispersion relation that describes the relation between wave frequency and wavevector (e.g., Stix 1992; Glassmeier et al. 1995; Zhao et al. 2020a). Different waves can be distinguished by the range of frequency or wavelength, wavevector direction, and polarization properties (i.e., characteristic correlations between velocity, magnetic field, and density fluctuations). For low-frequency magnetohydrodynamic (MHD) waves within the turbulent inertial range, the dominant Alfvén mode exhibits a transverse incompressible component with near-zero density fluctuations and magnetic field magnitude fluctuations (Velli et al. 1991). In contrast, fast and slow magnetosonic modes, which make up a small proportion of the total power, are compressible components, and the plasma density and magnetic field magnitude fluctuations are found to be positively correlated for fast waves and negatively correlated for slow waves (Howes et al. 2012).

In the dissipation range, where the turbulence energy begins to dissipate and is transferred into plasma thermal energy through wave–particle interactions, several different types of waves have been identified by in situ measurements, these being typically kinetic extensions of linear MHD modes. For example, quasi-parallel-propagating Alfvén/ion cyclotron waves (ICWs), which are believed to be closely related to the ion temperature anisotropy (Tu & Marsch 2002; Telloni et al. 2020), have a wavelength that corresponds roughly to the proton gyroradius and is left-hand polarized in the plasma rest frame (Jian et al. 2009, 2010; He et al. 2011a). Another common kinetic-scale wave mode are the oblique or quasi-perpendicular propagating kinetic Alfvén waves (KAWs), which can be described as a "coupling" between the Alfvén mode and the ion acoustic mode (and is thus more compressible than ICWs; Hollweg 1999). KAWs are right-hand-polarized fluctuations (He et al. 2011b; Podesta 2013) and are believed to be responsible for the observed steeper perpendicular-wavevector power spectra of magnetic fluctuations below the ion gyroscale (Leamon et al. 1999; Howes et al. 2008; Schekochihin et al. 2009). In contrast to the Alfvén wave mode, magnetosonic modes can propagate at/with frequencies above the proton gyrofrequency, such as the fast magnetosonic/whistler waves, which can exist at the electron gyroscale. Fast magnetosonic/whistler waves can propagate in a direction quasi-parallel (relatively incompressible) or very oblique (substantial magnetic compressibility) to the magnetic field

(Gary & Smith 2009). Quasi-parallel-propagating whistler waves are right-hand polarized, while highly oblique whistler waves are left-hand polarized, according to linear kinetic theory (He et al. 2011b). Kinetic plasma waves at the ion scale are also found to propagate mainly outward. The direction of propagation can be inferred from their magnetic polarization with respect to the background magnetic field direction in the spacecraft frame (Jian et al. 2009; He et al. 2011a). For example, quasi-parallel-propagating waves with a right-hand polarization in the spacecraft frame can be either fast magnetosonic/whistler waves that propagate with a right-hand polarization outward or ICWs propagating inward with a left-hand polarization in the solar wind frame (Woodham et al. 2019; Zhao et al. 2020a; Shi et al. 2021).

The Parker Solar Probe (PSP) has observed primarily magnetic-field-aligned flows and outward (or antisunward) propagating Alfvén waves in its first four orbits, with the normalized cross helicity being positive in the inward magnetic sector and negative in the outward magnetic sector (Zhao et al. 2021b). Inwardly propagating Alfvén waves and magnetosonic waves are minority populations during PSP's first encounter (Zhu et al. 2019). In situ observations show that the high Alfvénicity in the inner heliosphere tends to reduce with increasing distance from the Sun, i.e., the magnitude of the normalized cross helicity decreases with heliocentric distance (Roberts et al. 1987, 1990). Such decay may be due to the nonlinear interaction between counterpropagating Alfvén waves (Verdini & Velli 2007; Howes & Nielson 2013), or the coupling of the convected magnetic structures (i.e., quasi-2D fluctuations) with outward-propagating Alfvén waves (Tu & Marsch 1993; Bruno et al. 2003; Adhikari et al. 2017; Zank et al. 2017, 2020), or a nonlinear parametric decay process in which a unidirectional large-amplitude Alfvén wave decays into a counterpropagating small-amplitude daughter Alfvén wave with a smaller wavevector and a compressive wave (i.e., slow mode) propagating in the same direction as the pump wave (Tu et al. 1989; Malara & Velli 1996; Ofman & Davila 1997, 1998; Bruno et al. 2014; He et al. 2019). The reduction in Alfvénicity with increasing radial distance can also be an observational consequence of the more azimuthal interplanetary magnetic field farther away from the Sun, enabling easier measurements of the 2D fluctuations (Adhikari et al. 2017; Zank et al. 2017, 2020). During the first perihelion, PSP was connected to a small equatorial coronal hole and observed a highly Alfvénic slow solar wind, in which electron- and ion-scale waves generated through plasma instabilities were observed at distances close to 0.17 au (Bale et al. 2019). The statistical study based on the first encounter measurements indicates that about 30%–50% of radial field intervals have transverse circularly polarized ion-scale waves that may be driven by temperature anisotropy, suggesting that ion cyclotron resonance may play a role in dissipative coronal heating and hence solar wind acceleration (Bowen et al. 2020). During PSP's second orbit, SPAN-*i* and FIELDs measurements identified the simultaneous existence of proton beams and ion-scale waves, providing evidence for kinetic-scale wave–particle interactions (Verniero et al. 2020).

The Parker spiral magnetic field model (Parker 1958) suggests that the interplanetary magnetic field is more likely to be radial close to the Sun. Thus, the highly Alfvénic features of solar wind turbulence observed by PSP provide us a favorable opportunity to explore the properties of parallel/antiparallel-propagating fluctuations. Our previous work assumes that the wavevector is in the direction of the flow speed and has analyzed the spectral features of this class of turbulence with parallel wavevector $k_{\parallel}$ using PSP measurements (Zhao et al. 2020b), which yields a Kolmogorov-like $k_{\parallel}$ spectrum for magnetic field fluctuations in the inertial range. The $-5/3$ power spectrum in highly imbalanced turbulence with unidirectional Alfvén waves cannot be easily explained by earlier theories such as critical balance because of the diminishing nonlinearity. Zank et al. (2020) provide an explanation based on the nearly incompressible (NI) MHD theory where the unidirectional Alfvén wave is a minority component (i.e., slab turbulence) of the total fluctuations interacting nonlinearly in a passive sense with advected quasi-2D structures. In this paper, we present a detailed analysis of the characteristic wave modes in these field-aligned intervals, including both MHD and kinetic scales. The outline of the paper is as follows. Section 2 describes the methods used to estimate the wavevector and decompose the low-frequency MHD waves. Section 3 presents an overview of the two field-aligned intervals observed by PSP during its first two encounters. The identified MHD wave modes and their possible kinetic extension in these intervals are presented. Section 4 provides a summary and discussions.

2. Methods

In general, any wave mode can be described in terms of its dispersion relation (frequency and wavevector) and its polarization state (the internal magnetic field and plasma properties) (Jones 1988; Glassmeier et al. 1995). The wavevector $\boldsymbol{k}$ can be estimated according to the elementary condition $\boldsymbol{k}\cdot\delta\boldsymbol{B}=0$. Assuming that the magnetic fluctuation $\delta\boldsymbol{B}$ lies in a plane approximately, the minimum variance direction of the magnetic field is usually regarded as the wavevector direction since it is perpendicular to the $\delta\boldsymbol{B}$. For spectral analysis, Santolík et al. (2003) suggest a method of determining a frequency-dependent wavevector based on singular value decomposition (SVD). The basic idea is to find the $\boldsymbol{k}$ such that $\mathsf{S}\cdot\boldsymbol{k}=0$, where $S_{ij}=\langle\tilde{B}_i\tilde{B}_j^{*}\rangle$ is the spectral tensor. $\tilde{\boldsymbol{B}}$ is the Fourier transform of the magnetic field $\boldsymbol{B}$. The asterisk denotes the complex conjugate, and $\langle\rangle$ represents the ensemble average. As components of $\boldsymbol{k}$ are real numbers, the condition can be written as $\mathsf{A}\cdot\boldsymbol{k}=0$, where

$$\mathsf{A}=\begin{pmatrix}\Re S_{11} & \Re S_{12} & \Re S_{13}\\ \Re S_{12} & \Re S_{22} & \Re S_{23}\\ \Re S_{13} & \Re S_{23} & \Re S_{33}\\ 0 & -\Im S_{12} & -\Im S_{13}\\ \Im S_{12} & 0 & -\Im S_{23}\\ \Im S_{13} & \Im S_{23} & 0\end{pmatrix}.$$

Here $\Re S_{ij}$ is the real part of the cross spectrum and $\Im S_{ij}$ is the imaginary part. Since the system is overdetermined in general, the SVD of the matrix A provides the solution in the least-squares sense. By using the SVD method, the wavevector $\boldsymbol{k}$ is given by the "eigenvector" (row vector) that corresponds to the smallest singular value λ_1. The ellipticity of the polarization of the plasma wave is then estimated by $\zeta=\lambda_2/\lambda_3$, with λ_2 being the intermediate singular value and λ_3 the largest singular value. Linear polarization is indicated by ζ being close to 0 and circular polarization by ζ close to 1 assuming that $\lambda_1\ll\lambda_2$.

Another estimator is the so-called degree of polarization, which is defined as $P = \lambda_3/(\lambda_1 + \lambda_2 + \lambda_3)$ (Santolík et al. 2001). From these two parameters, the relationship between the three singular values can be obtained, which gives the polarization characteristics of waves. Compared to the minimum variance analysis (Sonnerup & Cahill 1967), the SVD method provides more comprehensive information on the scale dependence of the underlying fluctuations. We note that the SVD method determines the direction of the wavevector but does not distinguish between parallel/antiparallel directions. Although the method was developed for Fourier spectral analysis (Santolík et al. 2003), it can be applied to wavelet analysis by considering a time t and scale s dependent spectral matrix. In order to determine the wave propagation direction $\boldsymbol{k}(s, t)$ with respect to the background magnetic field $\boldsymbol{B_0}$, we use the envelope of the Morlet wavelet function to calculate the local mean magnetic field (e.g., Horbury et al. 2008; Podesta 2009),

$$\boldsymbol{B}_0(s, t_n) = \sum_m \boldsymbol{B}(t_m) \exp\left[-\frac{(t_n - t_m)^2}{2s^2}\right]. \quad (1)$$

Based on the wavevector $\boldsymbol{k}(s, t)$ obtained from the SVD method and the local mean magnetic field $\boldsymbol{B}_0(s, t)$, the wave propagation angle $\theta_{\boldsymbol{k},\boldsymbol{B}_0}$ can be determined, which also depends on both scale s and time t. To diagnose the MHD waves from single-point plasma and field measurements, we use the mode decomposition method developed by Glassmeier et al. (1995) to identify the three MHD waves, i.e., Alfvén waves, fast waves, and slow waves. This method has been widely used to detect the MHD wave modes (Motschmann et al. 1998; Narita & Marsch 2015; Chaston et al. 2020; Zhu et al. 2020). Based on the MHD eigenrelation, any arbitrary fluctuating magnetic field $\delta\boldsymbol{B}$, fluctuating velocity $\delta\boldsymbol{V}$, and fluctuating density $\delta\rho$ can be uniquely decomposed into the three MHD modes propagating in the forward and backward directions (relative to $\boldsymbol{B}_0$) by introducing the dimensionless state vector (Glassmeier et al. 1995):

$$\boldsymbol{\Gamma} \equiv \frac{1}{V_A}\left[\delta V_y, \frac{\delta B_y}{\sqrt{\mu_0\rho_0}}, \delta V_x, \delta V_z, \frac{\delta B_z}{\sqrt{\mu_0\rho_0}}, \frac{\delta\rho C_s}{\rho_0}\right]^T, \quad (2)$$

where the superscript T denotes transpose. The x-axis is defined along the wavevector $\boldsymbol{k}$ direction so that $\delta B_x = 0$ by assumption, the background magnetic field $\boldsymbol{B}_0$ lies in the x-z plane, and the y-axis is determined by right-hand orthogonality. Here ρ_0 is the mean mass density, V_A is the Alfvén speed, and C_s is the sound speed. Similar to the calculation of the local mean magnetic field $\boldsymbol{B_0}$, we can compute the scale- and time-dependent mean mass density ρ_0 and mean temperature T_0 (to evaluate the sound speed C_s). In this paper, we assume that the electron temperature T_e is approximately equal to the ion temperature T_i with no temperature anisotropy following a previous observational study from the PSP's first perihelion (Chaston et al. 2020), which shows that the uncertainty in wave recognition caused by these assumptions is much smaller than the observed changes in wave composition. From the state vector $\boldsymbol{\Gamma}$, the spectral energy contribution of the ith MHD mode is estimated by $|g_i|^2 = e_i^T S(f_{sc}, t) e_i$, where e_i is the eigenvector. $S(f_{sc}, t) = \boldsymbol{\Gamma}\boldsymbol{\Gamma}^*$ is the spectral density matrix, with $\boldsymbol{\Gamma}^*$ the conjugate transpose of $\boldsymbol{\Gamma}$. Therefore, the input parameters of MHD mode decomposition (Glassmeier et al. 1995) are the background parameters ($\boldsymbol{B}_0$, ρ_0, T_0), the fluctuating quantities ($\delta\boldsymbol{B}$, $\delta\boldsymbol{V}$, $\delta\rho$), and the propagation angle $\theta_{\boldsymbol{k},\boldsymbol{B}_0}$. In this work, we use the normalized form $|g_i|^2 \Big/ \sqrt{\sum_{j=1}^{6}|g_j|^2}$ to evaluate the fractional contribution of each MHD wave mode.

3. Data Overview and Results

We reanalyze the two field-aligned intervals observed by PSP during its first two orbits. Our previous study (Zhao et al. 2020b) selected these highly field-aligned intervals by limiting the angle between magnetic field and flow velocity. We have roughly estimated that the two intervals are dominated by strongly imbalanced unidirectional Alfvén waves owing to the high value of the normalized cross helicity σ_c (close to 1). However, fast or slow magnetosonic waves can also possess a large value of σ_c (e.g., He et al. 2015). In addition, the magnetic field power spectra exhibit a clear bump near the proton cyclotron frequency in both intervals (Zhao et al. 2020b), indicating the existence of kinetic plasma waves at the ion scale. In this work, we focus on the detailed identification of the wave modes in both intervals. The wavevector is estimated from the SVD method, the MHD wave modes are identified by the mode recognition method based on their dispersion relations, and the kinetic plasma waves are identified through their propagation direction and polarization properties in the spacecraft frame.

The data sets that we use are the Level 2 magnetic field data measured by the PSP/FIELDs/MAG instrument (Bale et al. 2016) and Level 3 plasma data measured by the PSP/SWEAP/SPC instrument (Kasper et al. 2016). We select a 1 hr interval centered at the field-aligned flow to conduct our wave mode recognition. Figure 1 shows an overview of the magnetic field and plasma variables observed in these two intervals. The first interval (left panels) was recorded on 2018 November 3, 04:00–05:00 UT at a radial distance of ~0.19 au and the second interval (right panels) on 2019 April 4, 05:00–06:00 UT with a radial distance of approximately 0.17 au. Here we average all the measurements down to a 10 s cadence to smooth the curve.

As shown in the top three panels, the magnetic field $\boldsymbol{B}$ is highly correlated with the flow speed $\boldsymbol{V}$ in both intervals. For the interval on 2018 November 3, the correlation coefficients (CCs) between the three vector component pairs, (B_R, V_R), (B_T, V_T), (B_N, V_N), are 0.84, 0.95, and 0.99, respectively. For the interval on 2019 April 4, $CC_{B_R,V_R} = 0.69$, $CC_{B_T,V_T} = 0.87$, $CC_{B_N,V_N} = 0.93$. The correlations between $\boldsymbol{V}$ and $\boldsymbol{B}$ in tangential and normal directions are much higher than that in the radial direction. The positive correlation also indicates that the observed underlying fluctuations are mainly Alfvénic waves propagating antiparallel to the mean magnetic field. As the magnetic field is in the sunward direction ($B_R < 0$) for both intervals, these Alfvén waves are propagating essentially outward/antisunward in the solar wind frame. The proton density fluctuations are relatively small, with $\delta\rho/\rho_0$ about 0.1 during the first interval and ~0.07 in the second interval. The proton temperature T_p is well correlated with the radial flow speed V_R during the second interval with $CC_{T_p,V_R} = 0.74$, which is consistent with the well-known linear relationship between the two quantities in the inner heliosphere (Elliott et al. 2012). However, T_p and V_R in the first interval are poorly

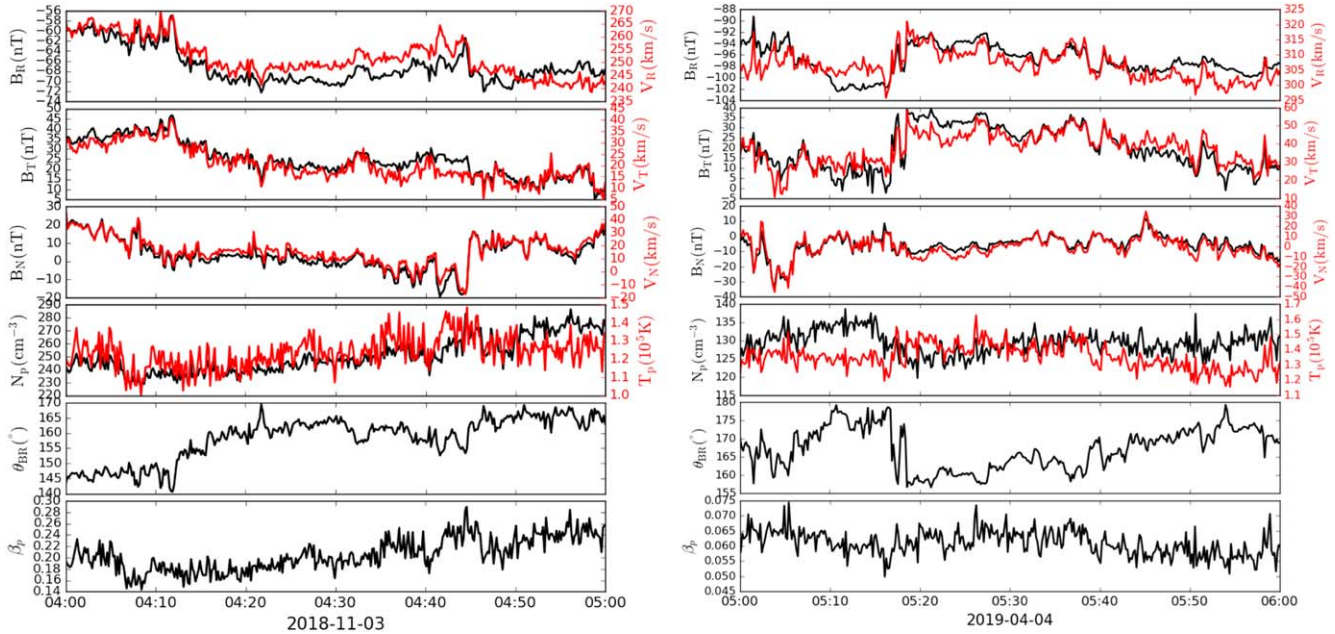

Figure 1. An overview of the PSP magnetic field and plasma measurements during 04:00–05:00 UT on 2018 November 3 (left panels) and during 05:00–06:00 UT on 2019 April 4 (right panels). The panels from top to bottom show the magnetic field vector (B_R, B_T, B_N), plasma velocity (V_R, V_T, V_N), proton density N_p, proton temperature T_p, the angle between the magnetic field and the radial direction $\theta_{\boldsymbol{BR}}$, and proton plasma beta β_p.

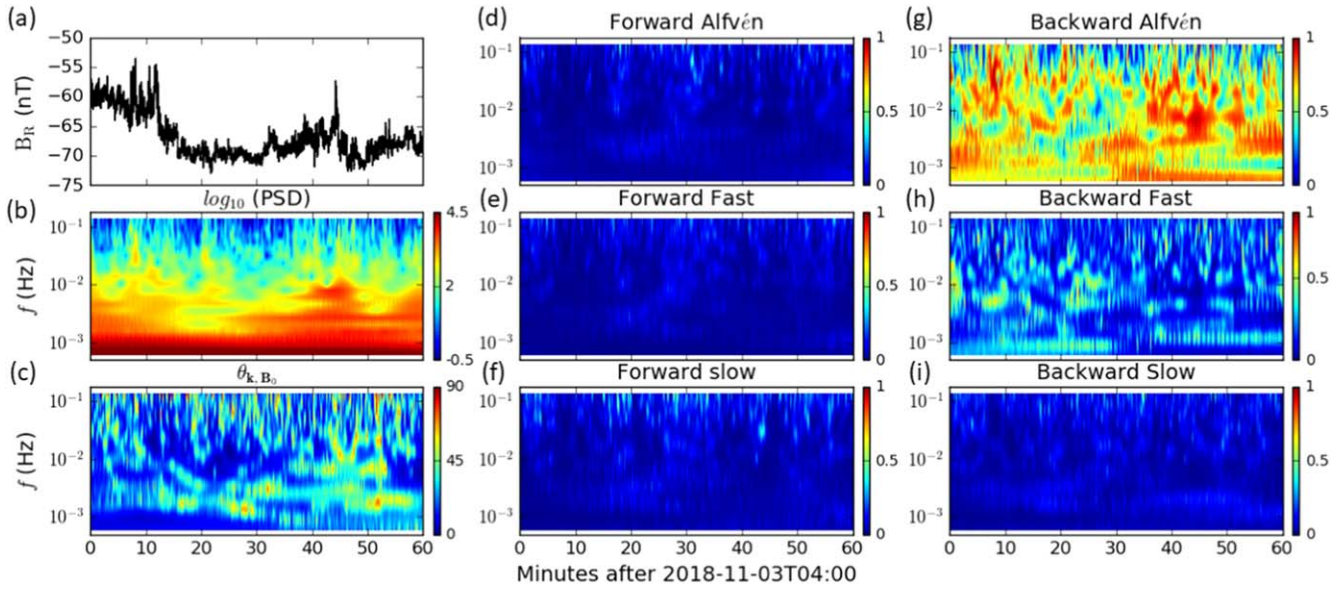

Figure 2. MHD mode decomposition during 04:00–05:00 UT on 2018 November 3. (a) Magnetic field radial component B_R. (b) PSD of the total magnetic field fluctuations. (c) Angle between wavevector $\boldsymbol{k}$ (determined from the SVD method) and the scale-dependent local background magnetic field $\boldsymbol{B_0}$. (d–i) The relative fraction of spectral energy density in each MHD wave mode.

correlated with $CC_{T_p,V_R} = -0.17$. The magnetic field is less aligned with the radial direction during the first interval, as indicated by the angle $\theta_{\boldsymbol{BR}}$, and the field-aligned flow starts from ∼04:15 UT (Zhao et al. 2020b). The proton plasma beta β_p shows no significant variation during both intervals, and it is much lower in the second interval (less than 0.1).

Figure 2 shows the MHD mode composition diagnosis in the first interval on 2018 November 3. Here the magnetic field components and plasma parameters have been averaged to 0.22 s cadence. Panel (a) shows the time profile of the B_R component with $B_R < 0$, indicating a sunward-oriented background magnetic field. Panel (b) shows the power spectral density (PSD) of the magnetic field fluctuations $\delta\boldsymbol{B}$ calculated from the wavelet method (Torrence & Compo 1998). The proton cyclotron frequency in the plasma frame is around 1.1 Hz for this interval. We analyze the fluctuation frequency in the range from $\sim 10^{-3}$ to 10^{-1} Hz, which corresponds to the MHD scale. In panel (c), we employ the SVD method to analyze the time series of $\delta\boldsymbol{B}$ to estimate the wavevector $\boldsymbol{k}$ direction. The local mean magnetic field $\boldsymbol{B_0}$ direction is determined by Equation (1). The angle between $\boldsymbol{k}$ and $\boldsymbol{B_0}$ is denoted as $\theta_{\boldsymbol{k},\boldsymbol{B_0}}$, which depends on both time and frequency. In general, $\theta_{\boldsymbol{k},\boldsymbol{B_0}}$ is mostly less than 45° in the considered frequency range (10^{-3}–10^{-1} Hz), suggesting that the MHD waves propagate in the direction quasi-parallel to the local mean magnetic field during this interval.

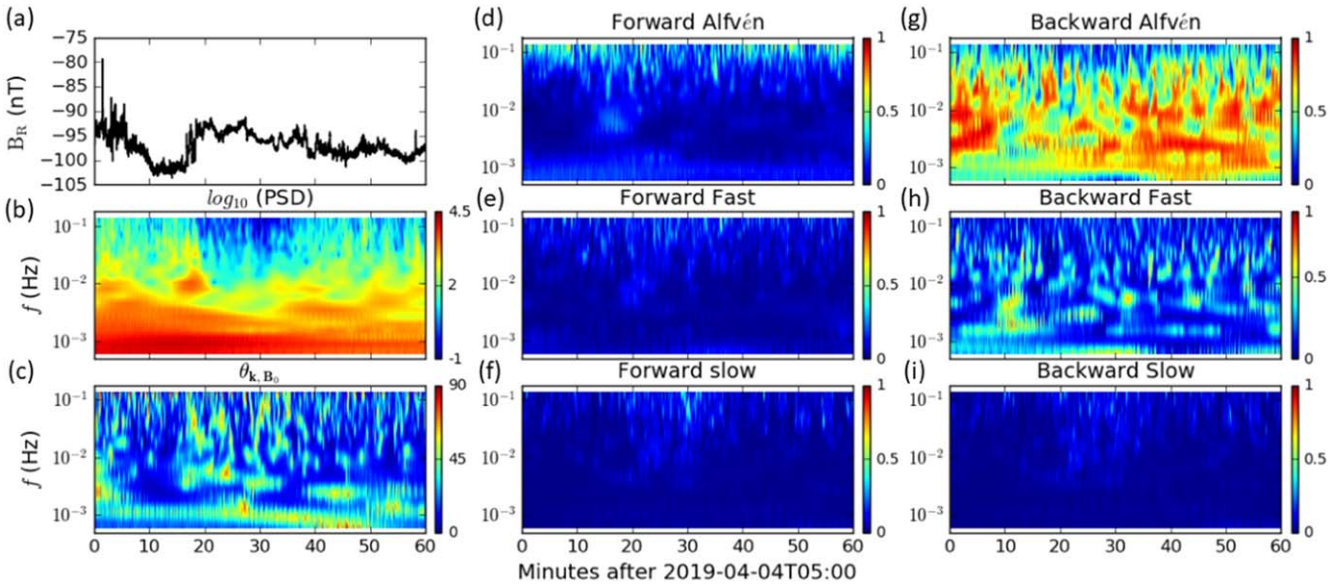

Figure 3. Same as Figure 2, but for the second field-aligned interval during the time period 05:00–06:00 UT on 2019 April 4.

Panels (d)–(i) show the fractional contribution to the spectral energy density of the six MHD modes as a function of frequency and time. Evidently, the backward (antiparallel to $\boldsymbol{B}_0$) propagating Alfvén wave is the dominant wave mode at all times and scales considered. Due to the negative B_R in the interval, the backward waves denote outward propagation (away from the Sun) and forward waves inward propagation (toward the Sun). Among other minority MHD modes, the backward fast mode has the largest contribution. The spectral contribution from the three forward modes is much less than in the backward-propagating modes over the considered frequency range. This appears different from earlier statistical results by Zhu et al. (2020) that suggest that the outward fast mode is typically the weakest among the six. The reason may be that, in their statistical study, they did not exclude "field-reversal" or "switchback" patterns that exist at various scales (Bale et al. 2019; Kasper et al. 2019). The intervals shown here are not contaminated by any "switchback" events and are typical field-aligned intervals with a low level of intermittency (Zhao et al. 2020b).

The MHD wave recognition technique is also applied to the second interval during 05:00–06:00 UT on 2019 April 4, and results are shown in Figure 3. The results are similar to the first interval. The proton gyrofrequency for this interval is around 1.5 Hz in the plasma frame. The negative B_R indicates that the backward (forward) waves are essentially propagating outward (inward). The trace power in the magnetic field fluctuations shows the corresponding enhancements when the time series data exhibit large fluctuations. The wavevector $\boldsymbol{k}$ is quasi-parallel to the local mean magnetic field over the considered frequency range. The outward-propagating Alfvén wave dominates, and the outward-propagating fast mode has the second-largest contribution. The spectral contribution from the three inward (forward) propagating modes is still minor compared to the outward (backward) propagating modes. We note that the fraction of the inward-propagating Alfvén mode increases at high frequencies (~0.1 Hz), which may be caused by instrumental noise inherent in the SPC data (Case et al. 2020), resulting in a flattening of the density fluctuation spectrum at high frequencies.

To examine possible kinetic wave activity, we further analyze high-resolution magnetic field measurements. In Figure 4, we use magnetic field data with a time resolution of 0.007 s to investigate fluctuations at frequencies near the proton kinetic scales. The left panel shows the frequency-dependent magnetic trace spectrum (top) and magnetic compressibility C_B (bottom) during the period 04:15–04:45 UT on 2018 November 3. The calculation of magnetic compressibility C_B is based on the method proposed by Bavassano et al. (1982). The right panel is for the interval on 2019 April 4, 05:20–05:50 UT. Both intervals lie in quiet periods without "field-reversal" events and show strict field alignment, with the averaged θ_{BR} being larger than 160°. The black lines show results from the standard Fourier transform method, and the red filled circles result from the Morlet wavelet transform (Zhao et al. 2021a). The wavelet spectrum is obtained by integrating the wavelet spectrogram over the time domain. The results from both methods are consistent. The proton cyclotron frequencies in the plasma frame f_c and in the spacecraft frame f_c^s are displayed as reference. The frequency f_c increases with decreasing heliocentric distance owing to the increased magnetic field strength.

The trace spectra of the magnetic field fluctuations in both intervals show a clear enhancement near the proton gyroscales (dashed lines). Correspondingly, the magnetic compressibility C_B drops near the spectral bump. These signatures indicate the presence of parallel/antiparallel-propagating kinetic plasma waves. The inertial-range spectra at frequencies smaller than f_c for both intervals exhibit a power-law shape that is close to the Kolmogorov $-5/3$ scaling. At frequencies larger than f_c^s, other spike-like enhancements are present in the spectra, which may be related to instrumental noise, and the subsequent spectra generally follow an f^{-1} scaling.

To further analyze the nature of the waves observed near the proton gyroscales, we analyze the magnetic field fluctuations with a cadence of ~0.007 s using the SVD method and the local mean magnetic field $\boldsymbol{B_0}$ calculation. Figure 5 shows several parameters related to the kinetic wave mode analysis within a period ranging from 0.1 to 10 s for the interval on 2018 November 3. The time period p is related to the wavelet

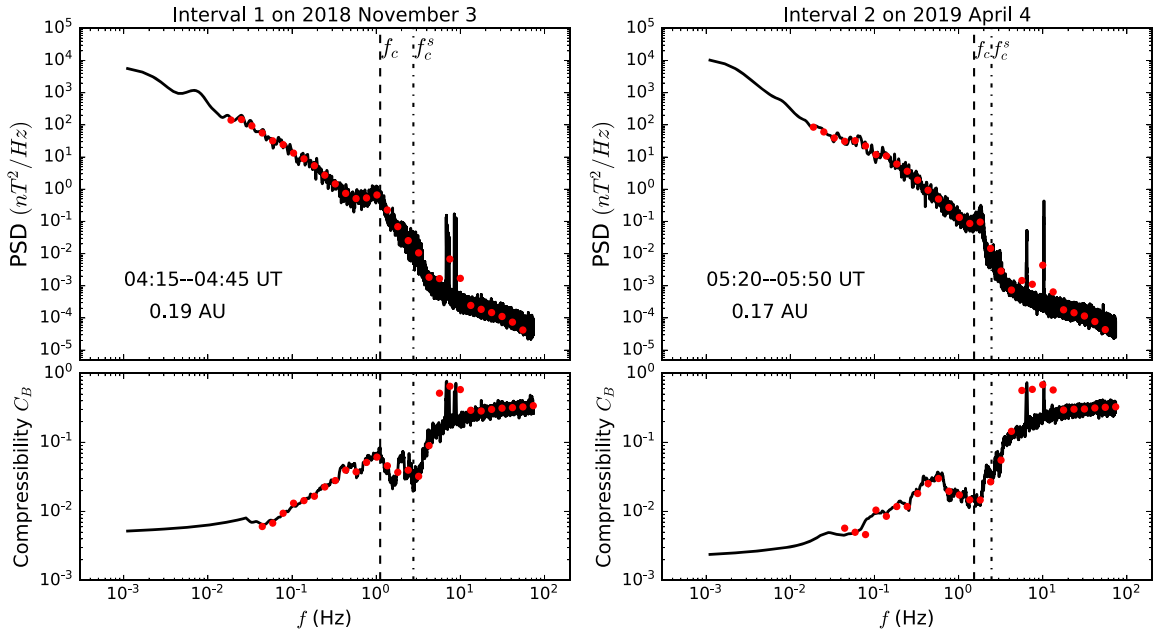

Figure 4. Top panels show the magnetic field trace power spectra for the interval on 2018 November 3 (left) and the interval on 2019 April 4 (right). Bottom panels show the corresponding magnetic compressibility C_B for each interval. The black lines represent the standard Fourier method, and the red filled circles denote results from the Morlet wavelet technique. f_c and f_c^s denote the proton cyclotron frequency in the plasma frame and in the spacecraft frame, respectively.

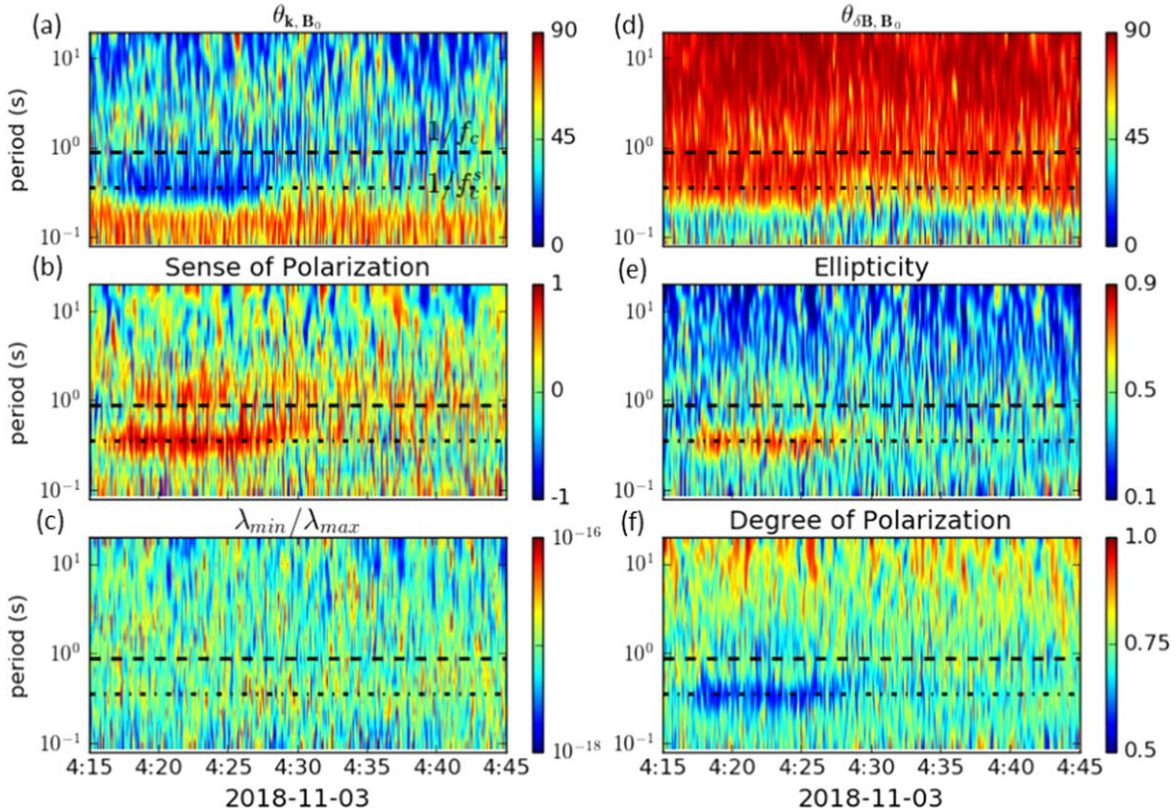

Figure 5. Analysis of wave modes using the SVD method and the local mean magnetic field method. (a) Spectra of the angle between the wavevector $\boldsymbol{k}$ and the local mean magnetic field $\boldsymbol{B_0}$. (b) The sense of magnetic polarization about $\boldsymbol{B_0}$ in the spacecraft frame. (c) The distribution of the ratio between the smallest and largest singular values. (d) Spectra of the angle between the fluctuating magnetic field $\delta\boldsymbol{B}$ and the local mean magnetic field $\boldsymbol{B_0}$. (e) The distribution of ellipticity of the polarization. (f) The distribution of degree of polarization.

scale s through $p \sim 1.03$ s. The horizontal dashed and dotted lines correspond to the proton cyclotron period/frequency in the plasma frame and in the spacecraft frame, respectively. The wavevector $\boldsymbol{k}$ direction is calculated using the SVD method described in Section 2. The sense of magnetic polarization shown in panel (b) is estimated through the cross spectrum

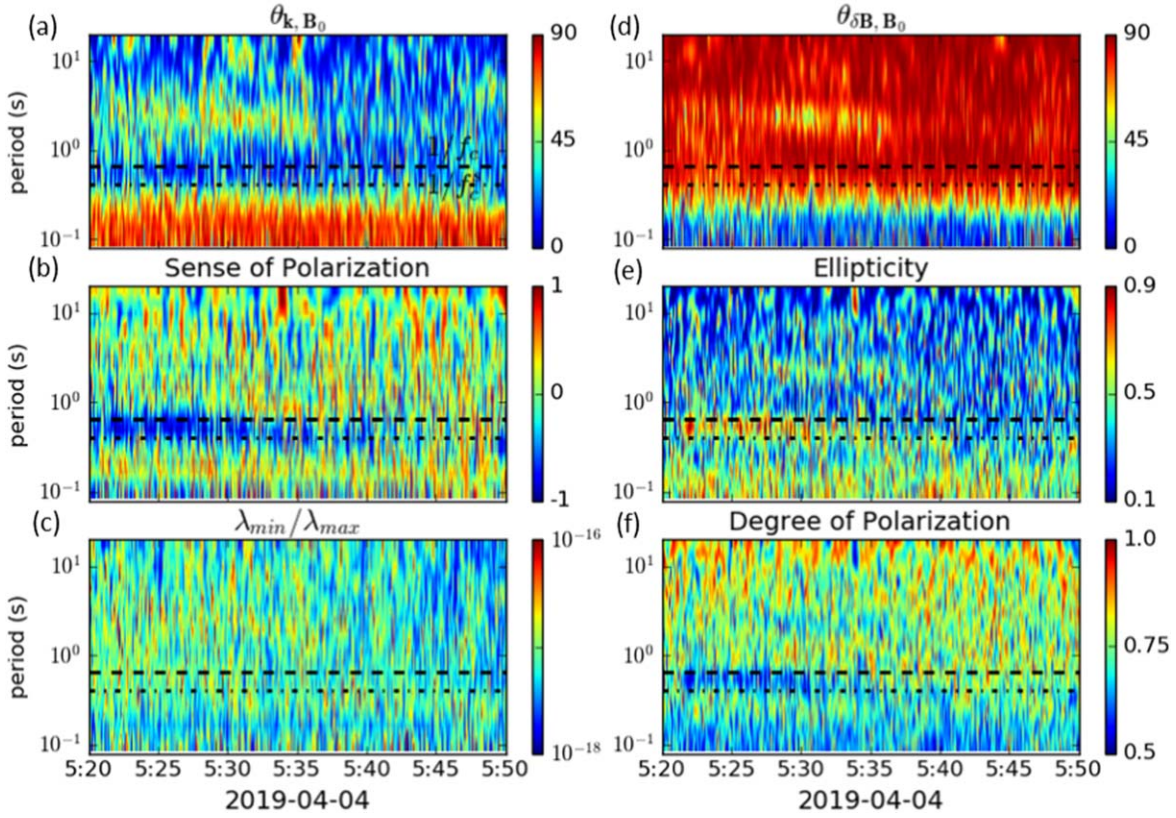

Figure 6. Same as Figure 5, but for the interval on 2019 April 4, 05:20–05:50 UT.

between the two orthogonal magnetic components in the plane perpendicular to $\boldsymbol{B_0}$ (Santolík et al. 2001), with values of -1 and 1 representing left- and right-hand polarization in the spacecraft frame. In the vicinity of the proton gyroscale, there are clear signals of kinetic plasma waves at the leading edge of the interval (∼4:15–4:30 UT), which results in the spectral bump near the proton cyclotron frequency shown in the left panel of Figure 4. This ion-scale plasma wave is characterized by the following features: (1) small $\theta_{\boldsymbol{k},\boldsymbol{B}_0}$, indicating that the wave propagates in a direction parallel or antiparallel to the local mean magnetic field; (2) large $\theta_{\delta\boldsymbol{B},\boldsymbol{B}_0}$, indicating that the fluctuations are dominated by incompressible transverse magnetic oscillations; (3) right-hand magnetic polarization about $\boldsymbol{B}_0$ in the spacecraft frame at scales near the proton gyrofrequency; and (4) nearly circular polarization ($\lambda_3 \simeq \lambda_2 \gg \lambda_1$). Since the bulk flow propagates antiparallel to the background magnetic field (negative B_R in Figure 2(a)), the identified right-hand polarization in the spacecraft frame can be either a forward (inward) propagating Alfvén/ICW or a backward (outward) propagating fast magnetosonic/whistler wave in the plasma frame (Zhao et al. 2020a). Due to the limited resolution of plasma measurements, we cannot determine the propagation direction (parallel or antiparallel to $\boldsymbol{B_0}$) of the identified kinetic wave by using the correlation between the magnetic field and velocity fluctuations to further confirm the exact wave mode. At the period smaller than $1/f_c^s$ (horizontal dotted lines), the wavevector appears to be perpendicular to $\boldsymbol{B}_0$, and the fluctuating magnetic field $\delta\boldsymbol{B}$ is dominated by the parallel compressible component, which is caused by the instrumental noise corresponding to the spike-like enhancements at high frequencies shown in the magnetic field trace spectrum (Figure 4).

Figure 6 shows a similar analysis to that in Figure 5 for the second field-aligned interval on 2019 April 4. The strong wave activity near the proton gyrofrequency is also associated with (1) small $\theta_{\boldsymbol{k},\boldsymbol{B}_0}$ (parallel or antiparallel), (2) $\theta_{\delta\boldsymbol{B},\boldsymbol{B}_0}$ close to 90° (dominant incompressible transverse fluctuations), and (3) nearly circular polarization as inferred from the relationship between the three singular values from panels (c), (e), and (f).

However, the sense of magnetic polarization in Figure 6(b) is opposite to that in the interval on 2018 November 3, although the background magnetic field points toward the Sun in both intervals. The ion-scale wave identified in this interval at around 1.5–2.5 Hz possesses a left-hand polarization in the inward magnetic sector, which can be either a backward (outward) propagating Alfvén/ICW or a forward (inward) propagating fast magnetosonic/whistler wave in the plasma frame (Zhao et al. 2020a; Shi et al. 2021).

Figure 7 shows the PSD of the magnetic field fluctuations at around 0.19 au covering the entire frequency range from the energy-containing range to the dissipation range. Some irrelevant instrumental noise signals are present at high frequencies ($f > f_{d_p}$). A Kolmogorov $f^{-5/3}$ spectrum is shown in the turbulent inertial range ($f_{\tau_c} < f < f_{\rho_p}$), justifying the use of the Kolmogorov estimate for the dissipation/heating rate by Zank et al. (2018) and Adhikari et al. (2020, 2021b), in which they have demonstrated that turbulence cascade is sufficient to heat the corona and drive the solar wind based on the agreement between the model and the observed plasma parameters, turbulence energy, cross helicity, residual energy, and correlation lengths of the Elsässer variables in the solar wind.

To evaluate the total energy density of the observed ion-scale waves, we integrate the PSD of magnetic field fluctuations

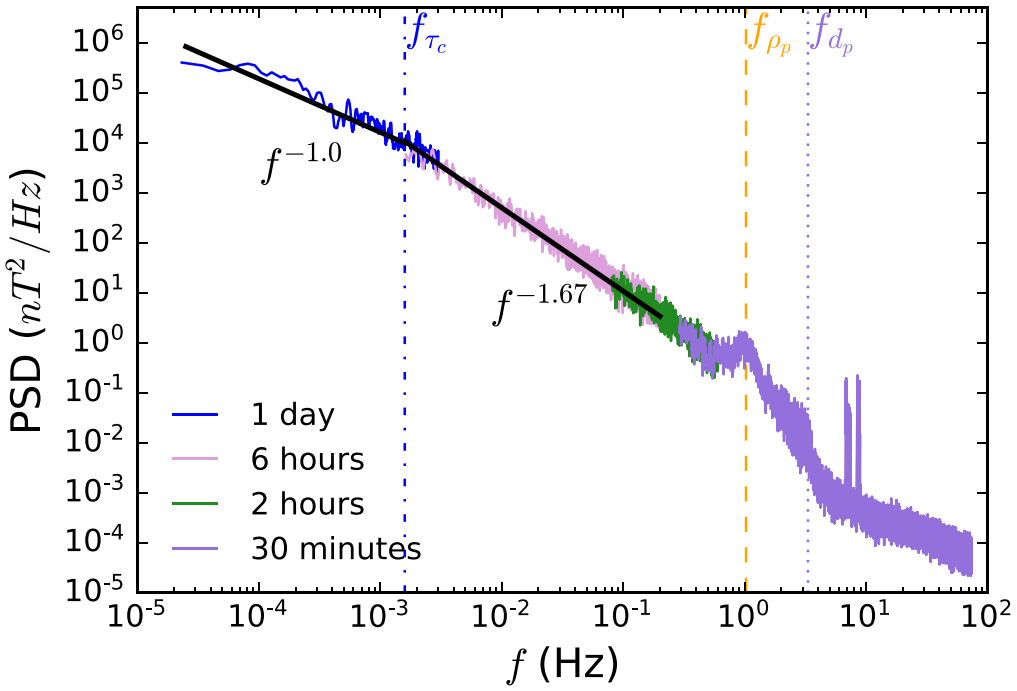

Figure 7. The magnetic field fluctuations trace power spectra using different intervals on 2018 November 3. f_{τ_c} denotes the frequency corresponding to the correlation scale, f_{ρ_p} represents the frequency corresponding to the proton gyroscale, and f_{d_p} is the frequency corresponding to the proton inertial length. f^{-1} and $f^{-5/3}$ power laws are displayed for reference.

(normalized to Alfvén units) over the frequency range from 0.5 to 4 Hz. Due to the limited resolution of plasma data, as an upper limit, we assume that the corresponding kinetic fluctuation energy is the same as that of the magnetic energy density. Then, the total energy density for the observed ion-scale waves $E_T^{\rm obs} \simeq 4.16$ km^2 s^{-2}. We compare it to the total turbulence energy predicted by the turbulence-driven solar wind model (Adhikari et al. 2020), i.e., $E_T^{\rm mod} \simeq 2 \times 10^4$ km^2 s^{-2} at $\sim$40 $R_\odot$. The ratio between $E_T^{\rm obs}$ and $E_T^{\rm mod}$ is about 0.0002. Evidently, the energy in ion-scale waves is dynamically negligible even after the turbulence energy introduced at the coronal base has dissipated and heated the corona to a temperature high enough to drive a supersonic solar wind (Adhikari et al. 2020). For MHD-scale waves, we integrate the PSD of magnetic field fluctuations and velocity fluctuations over the frequency range 10^{-3}–10^{-1} Hz to obtain their total energy density E_T for the studied MHD-scale waves, which is about 311 km^2 s^{-2}. The ratio between $E_T^{\rm obs}$ and $E_T^{\rm mod}$ for MHD waves is about 0.016. As before, the energy in MHD-scale waves in the solar wind is also negligible.

We point out that the results above do not mean that turbulence cannot drive the solar wind. The frequency regimes that we explore in this manuscript correspond to the cascade of turbulence from the energy-containing range (i.e., the inertial range) and its eventual dissipation (the ion-scale range). The important quantity is the rate at which energy cascades through this frequency range and is eventually dissipated, since if there is sufficient energy available in the energy-containing range and if it can be liberated to heat the plasma sufficiently rapidly, then the corona can be heated rapidly enough to form a solar wind. Hence, despite the small ratios of the energy in the ion-scale and MHD inertial ranges compared to the total energy in turbulent fluctuations, the results presented here illustrate the basic physics of the heating mechanism, i.e., a cascading of energy to smaller scales through the inertial range and then possibly eventual dissipation via ion-scale waves. However, the ion-scale wave part of the spectrum does not roll over exponentially (or as a steeper power law) as is typical of fluctuations in the dissipation range (e.g., Alexandrova et al. 2009). Instead, the figure shows clearly that the ion-scale waves we observe are excited/driven by some process (such as a beam) since they appear as an enhancement near the termination of the Kolmogorov spectrum. Thereafter, it seems that the dissipation range is more clearly observed at larger frequencies. So while the ion-scale waves may provide an additional heating mechanism, it should be regarded as supplementary to the primary heating process, which is the turbulent cascade and subsequent heating by small-scale fluctuations.

Finally, we estimate the turbulence cascade rate based on the formula derived through dimensional analysis (Adhikari et al. 2021a),

$$\epsilon = \frac{E_b^{3/2}}{[C_k \log(1/(k_{\rm inj}\lambda_b))]^{3/2}\,\lambda_b}, \tag{3}$$

where E_b denotes the turbulent magnetic energy in the energy-containing range, $C_k = 1.6$ is a Kolmogorov constant, $k_{\rm inj}$ is the wavenumber corresponding to the outer scale, and λ_b is the magnetic fluctuation correlation length. As shown in the figure, the correlation length scale ($\tau_c V_{\rm sw}$), which separates the energy-containing range and the inertial range, is around 1.7×10^5 km for a 1-day interval at 0.19 au. According to Equation (3), the dissipation rate in this 1-day interval is around 3×10^4 J kg^{-1} s^{-1}, which is consistent with the previous studies on turbulent energy cascade rate based on the Kolmogorov–Yaglom law using PSP observations (Bandyopadhyay et al. 2020) and the dissipation rates derived from the

Kolmogorov-based turbulence transport models (Zank et al. 2017, 2018; Adhikari et al. 2020, 2021a).

4. Discussions and Conclusions

We revisit two field-aligned solar wind intervals observed by PSP during its first two orbits. By Taylor's hypothesis, when the solar wind flow is aligned with the mean magnetic field, the observer will preferentially sample the slab component of the turbulence and observation of quasi-2D fluctuations will be suppressed (Zank et al. 2020). Our previous analyses found that these intervals are highly Alfvénic with the normalized cross helicity close to 1 and the magnetic field fluctuations possess approximately Kolmogorov-like scaling (Zhao et al. 2020b). The observed $-5/3$ scaling in unidirectional Alfvénic fluctuations can be explained by the NI MHD turbulence model (Zank et al. 2020). In NI MHD theory, the nonlinear interaction of the dominant 2D fluctuations does not require counterpropagating Alfvén waves. However, unidirectionally propagating Alfvén waves (and indeed slab turbulence with $|\sigma_c| \sim 1$) can couple nonlinearly and passively to advected quasi-2D turbulent structures via the combined nonlinear and Alfvénic timescales. The Kolmogorov scaling emerges from the 2D-dominated regime when the Alfvén timescale is longer than the 2D nonlinear timescale (Zank et al. 2020).

We utilize multiple techniques to analyze wave properties in the two field-aligned flow intervals. The more detailed analysis is a further step toward understanding the nature of turbulence in the solar wind. The SVD method is applied to obtain the wavevector direction based on the full wavelet spectral matrix of the magnetic field fluctuations. The MHD mode decomposition technique is used to identify the composition of six linear MHD waves (forward and backward Alfvén, fast, and slow modes) at low frequencies. For high-frequency fluctuations, polarization properties are used to determine the nature of kinetic waves.

Our new analysis strongly suggests the presence of wave activity at both MHD and ion kinetic scales. At MHD scales, we find that most of the fluctuation power is in the outward-propagating Alfvén mode, with a minor contribution from the outward-propagating fast mode. The MHD mode identification has been investigated in several previous studies. It is typically found that slow modes are the second most important wave component after the dominant Alfvén modes (e.g., Howes et al.2012; Chaston et al. 2020; Zhu et al. 2020), which is inconsistent with our findings. However, in the limit of perpendicular wavevector, the slow wave corresponds to an undamped nonpropagating pressure-balanced structure (Howes et al. 2012). Since those previous studies are not restricted to field-aligned flow intervals, it is likely that nonpropagating quasi-2D structures are included in the total fluctuations and are misclassified as propagating slow waves. Moreover, slow-mode-like fluctuations with quasi-perpendicular wavevectors and pressure-balanced characteristics are found to consist of two populations in 3D simulated MHD turbulence: one is related to propagating slow-mode waves and the other to nonpropagating slow-mode-like structures (Yang et al. 2017, 2018). Based on the NI turbulence model, it is expected that the nonpropagating quasi-2D structures contribute ~80% of the total fluctuation power (Zank et al. 2017, 2020) and thus have a major impact on the wave contribution analysis. In contrast, by restricting our analysis to intervals where the sampling direction is along the mean magnetic field, we are able to eliminate most of the 2D structures and focus on waves only.

The results of the MHD mode decomposition are of great importance in understanding the acceleration of solar wind. The outward Alfvénic nature of the observed fluctuations supports the Alfvén wave acceleration models such as discussed by Ofman & Davila (1997, 1998), Suzuki & Inutsuka (2005), Suzuki (2011), and the reviews by Ofman (2010, 2016) and Banerjee et al. (2021). Turbulence-driven solar wind models that rely on the nonlinear interactions of Alfvén waves require counterpropagating Alfvén waves (e.g., Goldreich & Sridhar 1995), which are not seen in our analysis. Since the observation is made in the super-Alfvénic solar wind, we cannot rule out Alfvénic turbulence due to reflection in the corona (e.g., Velli 1993; Matthaeus et al. 1999). Another class of turbulence models based on the NI theory do not require counterpropagating Alfvén waves to provide the nonlinearity (e.g., Zank et al. 2018; Adhikari et al. 2020). As we have discussed in the previous work (Zank et al. 2020; Zhao et al. 2020b), the observation of highly imbalanced Alfvénic turbulence with a Kolmogorov-type power spectrum is consistent with the NI model. A comprehensive discussion of the NI turbulence theory and supporting observations from PSP and Solar Orbiter is presented in Zank et al. (2021). We further caution that the observed wind speed in the present work is low (~300 km s^{-1}), suggesting that the intervals chosen here may not be best suited for studying the acceleration of fast wind (e.g., Ofman 2010). Future observations by Solar Orbiter may provide more insights into the acceleration of fast wind originating from the coronal holes.

At ion kinetic scales, we find that either inward-propagating ICWs or outward-propagating fast-mode/whistler waves are observed in the first interval, while either outward-propagating ICWs or inward-propagating fast-mode/whistler waves are observed in the second interval. Because of the limited plasma data resolution, the exact wave mode is difficult to identify. Ion-scale waves have been identified frequently in previous solar wind observations. The question about the origin of the ion-scale waves remains open. One possibility is that they are generated locally by an unstable particle distribution such as a beam or temperature anisotropy (e.g., Yoon 2017; Sun et al. 2019; Woodham et al. 2019; Verniero et al. 2020). The presence of kinetic waves may be a consequence of anisotropic heating of solar wind. For example, Isenberg et al. (2019) and Isenberg & Vasquez (2019) suggest that oblique KAWs preferentially heat the ions in the perpendicular direction and the quasi-parallel-propagating ICWs can be generated by the resulting temperature anisotropy. The preferential heating and acceleration of He^{++} and heavy ions may also be related to kinetic waves (e.g., Ofman 2010; Ofman et al. 2014, 2017; Navarro et al. 2020). Ion-scale waves are the subject of many previous PSP studies (e.g., Bowen et al. 2020; Perrone et al. 2020; Verniero et al. 2020; Shi et al. 2021). Based on the calculation of energy transfer rates from waves to particles, Vech et al. (2021) conclude that ICWs are generated locally in the solar wind. Evidence for unstable ion distributions observed by the PSP/SPAN-*i* instrument associated with ion-scale waves has also been reported (Verniero et al. 2020; Klein et al. 2021).

In this work, we identify both MHD and ion-scale waves in field-aligned flows using PSP measurements. There are two points that make our study different from previous work (e.g.,

Marsch et al. 1982; Tu & Marsch 1995, 2002). First, the present study extends to closer radial distances than any previous studies. We can make measurements of ion-scale waves at much closer distances and determine their properties. This is important because it distinguishes between Helios observations at 0.3 au and those made closer in by PSP. Second, we specifically consider highly field-aligned flows, which are free of contamination of 2D structures that may dominate the total fluctuation energy (e.g., Zank et al. 2021). We believe that none of the past studies have focused particularly on waves in field-aligned flows, and in fact the waves identified in non-field-aligned flows may be contaminated by 2D structures (Zhao et al. 2020a, 2021b). Our results are consistent with previous studies in some aspects, namely, the dominant outward-propagating Alfvén wave and ion-scale waves. However, the second important MHD mode in our study is the fast magnetosonic mode, which may be due to the field-aligned intervals we chose. The connection between the observed ion-scale waves and low-frequency MHD waves remains to be understood. The dominance of the incompressible Alfvén fluctuations over the fast-mode waves may be related to the NI theory that brings in the compressible fast mode as a higher-order contribution (Zank & Matthaeus 1993). In subsequent work, we will conduct a statistical study of wave composition in field-aligned flows observed by both PSP and Solar Orbiter and investigate their properties under different solar wind conditions, including solar wind speed, temperature, and plasma beta. This will help us better understand their generation processes and relation with the heating of the solar wind.

We acknowledge the partial support of the NSF EPSCoR RII-Track-1 Cooperative Agreement OIA-1655280, a NASA award 80NSSC20K1783, and a NASA Parker Solar Probe contract SV4-84017. We thank the NASA Parker Solar Probe SWEAP team led by J. Kasper and the FIELDS team led by S. D. Bale for use of data.

ORCID iDs

L.-L. Zhao https://orcid.org/0000-0002-4299-0490
G. P. Zank https://orcid.org/0000-0002-4642-6192
J. S. He https://orcid.org/0000-0001-8179-417X
D. Telloni https://orcid.org/0000-0002-6710-8142
L. Adhikari https://orcid.org/0000-0003-1549-5256
M. Nakanotani https://orcid.org/0000-0002-7203-0730
J. C. Kasper https://orcid.org/0000-0002-7077-930X
S. D. Bale https://orcid.org/0000-0002-1989-3596

References

Adhikari, L., Zank, G., Hunana, P., et al. 2017, ApJ, 841, 85
Adhikari, L., Zank, G., & Zhao, L. 2021a, Fluids, 6, 368
Adhikari, L., Zank, G., Zhao, L., Nakanotani, M., & Tasnim, S. 2021b, A&A, 650, A16
Adhikari, L., Zank, G. P., & Zhao, L.-L. 2020, ApJ, 901, 102
Alexandrova, O., Saur, J., Lacombe, C., et al. 2009, PhRvL, 103, 165003
Bale, S., Badman, S., Bonnell, J., et al. 2019, Natur, 576, 237
Bale, S. D., Goetz, K., Harvey, P. R., et al. 2016, SSRv, 204, 49
Bandyopadhyay, R., Goldstein, M., Maruca, B., et al. 2020, ApJS, 246, 48
Banerjee, D., Krishna Prasad, S., Pant, V., et al. 2021, SSRv, 217, 76
Bavassano, B., Dobrowolny, M., Mariani, F., & Ness, N. 1982, JGRA, 87, 3617
Belcher, J., & Davis, L., Jr. 1971, JGR, 76, 3534
Bowen, T. A., Mallet, A., Huang, J., et al. 2020, ApJS, 246, 66
Bruno, R., Carbone, V., Sorriso-Valvo, L., & Bavassano, B. 2003, JGRA, 108, 1130
Bruno, R., Telloni, D., Primavera, L., et al. 2014, ApJ, 786, 53
Case, A. W., Kasper, J. C., Stevens, M. L., et al. 2020, ApJS, 246, 43
Chaston, C., Bonnell, J., Bale, S., et al. 2020, ApJS, 246, 71
Coleman, P. J., Jr. 1967, P&SS, 15, 953
Elliott, H., Henney, C., McComas, D., Smith, C., & Vasquez, B. 2012, JGRA, 117, A09102
Gary, S. P., & Smith, C. W. 2009, JGRA, 114, A12105
Glassmeier, K., Motschmann, U., & Stein, R. 1995, AnGeo, 13, 76
Goldreich, P., & Sridhar, S. 1995, ApJ, 438, 763
Goldstein, M. L., Roberts, D. A., & Matthaeus, W. 1995, ARA&A, 33, 283
He, J., Duan, D., Zhu, X., Yan, L., & Wang, L. 2019, ScChD, 62, 619
He, J., Marsch, E., Tu, C., Yao, S., & Tian, H. 2011a, ApJ, 731, 85
He, J., Pei, Z., Wang, L., et al. 2015, ApJ, 805, 176
He, J., Tu, C., Marsch, E., & Yao, S. 2011b, ApJL, 745, L8
Hollweg, J. V. 1999, JGRA, 104, 14811
Horbury, T. S., Forman, M., & Oughton, S. 2008, PhRvL, 101, 175005
Howes, G., Bale, S., Klein, K., et al. 2012, ApJL, 753, L19
Howes, G. G., Cowley, S. C., Dorland, W., et al. 2008, JGRA, 113, A05103
Howes, G. G., & Nielson, K. D. 2013, PhPl, 20, 072302
Isenberg, P. A., & Vasquez, B. J. 2019, ApJ, 887, 63
Isenberg, P. A., Vasquez, B. J., & Hollweg, J. V. 2019, ApJ, 870, 119
Jian, L., Russell, C., Luhmann, J., et al. 2010, JGRA, 115, A12115
Jian, L. K., Russell, C. T., Luhmann, J. G., et al. 2009, ApJL, 701, L105
Jones, T. 1988, ApJ, 332, 678
Kasper, J. C., Abiad, R., Austin, G., et al. 2016, SSRv, 204, 131
Kasper, J. C., Bale, S. D., Belcher, J. W., et al. 2019, Natur, 576, 228
Klein, K., Verniero, J., Alterman, B., et al. 2021, ApJ, 909, 7
Leamon, R. J., Smith, C. W., Ness, N. F., & Wong, H. K. 1999, JGRA, 104, 22331
Malara, F., & Velli, M. 1996, PhPl, 3, 4427
Marsch, E., Goertz, C., & Richter, K. 1982, JGRA, 87, 5030
Matthaeus, W. H., Zank, G. P., Oughton, S., Mullan, D., & Dmitruk, P. 1999, ApJL, 523, L93
Motschmann, U., Glassmeier, K.-H., & Pinçon, J.-L. 1998, ISSIR, 1, 79
Narita, Y., & Marsch, E. 2015, ApJ, 805, 24
Navarro, R. E., Muñoz, V., Valdivia, J. A., & Moya, P. S. 2020, ApJL, 898, L9
Ofman, L. 2010, LRSP, 7, 1
Ofman, L. 2016, Low-Frequency Waves in Space Plasmas (New York: Wiley), 241
Ofman, L., & Davila, J. 1997, ApJ, 476, 357
Ofman, L., & Davila, J. 1998, JGRA, 103, 23677
Ofman, L., Denton, R., Bortnik, J., et al. 2017, JGRA, 122, 6469
Ofman, L., Viñas, A., & Maneva, Y. 2014, JGRA, 119, 4223
Parker, E. N. 1958, ApJ, 128, 664
Perrone, D., Bruno, R., D'amicis, R., et al. 2020, ApJ, 905, 142
Podesta, J. 2009, ApJ, 698, 986
Podesta, J. J. 2013, SoPh, 286, 529
Roberts, D., Goldstein, M., Klein, L., & Matthaeus, W. 1987, JGRA, 92, 12023
Roberts, D. A., Goldstein, M. L., & Klein, L. W. 1990, JGR, 95, 4203
Santolík, O., Lefeuvre, F., Parrot, M., & Rauch, J. 2001, JGRA, 106, 13191
Santolík, O., Parrot, M., & Lefeuvre, F. 2003, RaSc, 38, 1010
Schekochihin, A., Cowley, S., Dorland, W., et al. 2009, ApJS, 182, 310
Shi, C., Zhao, J., Huang, J., et al. 2021, ApJL, 908, L19
Sonnerup, B. Ö., & Cahill, L., Jr. 1967, JGR, 72, 171
Stix, T. H. 1992, Waves in Plasmas (Berlin: Springer Science & Business Media)
Sun, H., Zhao, J., Xie, H., & Wu, D. 2019, ApJ, 884, 44
Suzuki, T. K. 2011, SSRv, 158, 339
Suzuki, T. K., & Inutsuka, S.-i 2005, ApJL, 632, L49
Telloni, D., Bruno, R., D'Amicis, R., et al. 2020, ApJ, 897, 167
Torrence, C., & Compo, G. P. 1998, BAMS, 79, 61
Tu, C.-Y., & Marsch, E. 1993, JGRA, 98, 1257
Tu, C.-Y., & Marsch, E. 1995, SSRv, 73, 1
Tu, C.-Y., & Marsch, E. 2002, JGRA, 107, SSH
Tu, C.-Y., Marsch, E., & Thieme, K. 1989, JGRA, 94, 11739
Vech, D., Martinović, M., Klein, K. G., et al. 2021, A&A, 650, A10
Velli, M. 1993, A&A, 270, 304
Velli, M., Grappin, R., & Mangeney, A. 1991, GApFD, 62, 101
Verdini, A., & Velli, M. 2007, ApJ, 662, 669
Verniero, J., Larson, D., Livi, R., et al. 2020, ApJS, 248, 5
Woodham, L. D., Wicks, R. T., Verscharen, D., et al. 2019, ApJL, 884, L53
Yang, L., He, J., Tu, C., et al. 2017, ApJ, 836, 69
Yang, L., Zhang, L., He, J., et al. 2018, ApJ, 866, 41
Yoon, P. H. 2017, RvMPP, 1, 1

Zank, G., Adhikari, L., Hunana, P., et al. 2017, ApJ, 835, 147
Zank, G., Adhikari, L., Hunana, P., et al. 2018, ApJ, 854, 32
Zank, G., Nakanotani, M., Zhao, L.-L., Adhikari, L., & Telloni, D. 2020, ApJ, 900, 115
Zank, G., Zhao, L.-L., Adhikari, L., et al. 2021, PhPl, 28, 080501
Zank, G. P., & Matthaeus, W. 1993, PhFlA, 5, 257
Zhao, J., Wang, T., Graham, D. B., et al. 2020a, ApJ, 890, 17
Zhao, L., Zank, G., He, J., et al. 2021a, A&A, accepted
Zhao, L.-L., Zank, G., Adhikari, L., et al. 2020b, ApJ, 898, 113
Zhao, L.-L., Zank, G., Hu, Q., et al. 2021b, A&A, 650, A12
Zhu, X., He, J., Verscharen, D., Duan, D., & Bale, S. D. 2020, ApJL, 901, L3
Zhu, X., He, J., Verscharen, D., & Zhao, J. 2019, ApJ, 878, 48